International Journal of Enhanced Research in Educational Development (IJERED)
ISSN: 2320-8708, Vol. 14 Issue 5, September-October, 2026

Rare Earth Elements Doped Calcium Acuminate

Mr. Ninad Ramchandra Patil[1], Dr. Mohan Amrutrao Gaikwad[2]

[1]Sonopant Dandekar Arts, V. S. Apte Commerce and M. H. Mehta Science College Palghar. Maharashtra
[2]Gokhale Education Society's N. B. Mehta Science College Bordi, Maharashtra, India

DOI: https://doi.org/10.55948/IJERED.2026.0917

ABSTRACT

Rare-earth-doped calcium aluminate ($CaAl_2O_4$) is a promising phosphor due to its high chemical and thermal stability, low cost, and suitable luminescent properties. In this study, Eu^{3+}- and Dy^{3+}-doped $CaAl_2O_4$ phosphors with different dopant concentrations were synthesized and characterized using XRD, photoluminescence, UV–visible diffuse reflectance, and decay measurements. XRD confirmed a monoclinic $CaAl_2O_4$ phase with decreasing crystallite size at higher dopant concentrations. Eu^{3+} exhibited characteristic emission around 613 nm, along with a blue host/defect-related emission near 440 nm. Maximum luminescence occurred at approximately 3 mol% dopant concentration, followed by concentration quenching. The optical band gap decreased from approximately 5.30 to 5.15 eV with increasing dopant concentration. The results demonstrate that rare-earth-doped $CaAl_2O_4$ is a versatile material with potential applications in solid-state lighting, displays, safety signage, radiation dosimetry, and anti-counterfeiting technologies.

Keywords: Calcium aluminate, rare earth doping, photoluminescence, persistent luminescence, phosphor, europium, dysprosium, XRD, concentration quenching, solid-state lighting.

INTRODUCTION

Due to their widespread use in solid-state lighting, flat-panel and emissive displays, biomedical imaging probes, radiation dosimetry, anti-counterfeiting technology, and long-persistence safety and signage applications, phosphors are one of the most extensively researched functional materials in modern materials science. Nearly all viable phosphors have a crystalline host lattice with optically active dopant ions added at low concentration to form radiative recombination centers. Sulfides, silicates, phosphates, borates, aluminates, and complex oxynitrides have been studied, but the alkaline-earth aluminate family has garnered attention because it has several desirable and rare properties: high thermal and chemical stability, mechanical robustness, and a wide optical band gap that allows efficient host-to-dopant energy transfer. Calcium aluminate, found in the $CaAl_2O_4$ ($CaO{\cdot}Al_2O_3$) stoichiometry, and related polymorphs like $Ca_3Al_2O_6$, $CaAl_4O_7$, and $Ca_{12}Al_{14}O_{33}$, has a unique place within this family. $CaAl_2O_4$ crystallizes in a monoclinic framework (space group $P2_1/n$) with corner-sharing AlO_4 tetrahedra, forming a three-dimensional network with irregular, huge interstitial spaces for Ca^{2+} ions. Trivalent rare earth ions (RE^{3+}) can replace Ca^{2+} with moderate lattice distortion, creating a charge mismatch and the possibility of charge-compensation. Their ionic radii range from 0.86 Å (Lu^{3+}) to 1.16 Å (La^{3+}) in eight-fold coordination.

Rare earth metals, including the lanthanide family (La-Lu), scandium, and yttrium, have partially filled 4f electron shells sheltered from the crystal field by outer $5s^2$ and $5p^6$ orbitals. The shielding causes trivalent lanthanide ions to have narrow, line-like intra-configurational 4f–4f transitions whose energies are only weakly perturbed by the host lattice, unlike transition-metal activators' broad, host-sensitive d–d or charge-transfer bands. Several rare earth ions, including Ce^{3+}, Eu^{2+}, and to a lesser extent Pr^{3+} and Tb^{3+}, exhibit energy-dependent 4f–5d transitions, resulting in broad excitation and emission bands sensitive to local crystal-field strength and covalency. This property is used to tune emission color across the visible spectrum. Europium, a rare earth activator, may be used in oxide hosts in either trivalent (Eu^{3+}) or divalent (Eu^{2+}) oxidation states, depending on synthesis environment, host lattice chemistry, and charge-compensation needs. Eu^{3+} activation causes red-orange emission, dominated by the $^5D_0 \rightarrow {}^7F_2$ hypersensitive transition at 610-615 nm. This phenomenon is widely used in fluorescent lamps, plasma display panels, and phosphor-converted white light-emitting diodes. Eu^{2+} aluminates, such as $SrAl_2O_4:Eu^{2+},Dy^{3+}$, are known for their long-lasting green phosphor, with a broad emission band that can shift from near-ultraviolet to blue, green, and even yellow-orange depending on the host's crystal-field splitting and covalency.

Dysprosium, often used as a co-dopant with Eu^{2+} or Eu^{3+}, has a complimentary function. The optically active Dy^{3+} emits blue ($^4F_{9/2} \rightarrow {}^6H_{15/2}$, ~480 nm) and yellow ($^4F_{9/2} \rightarrow {}^6H_{13/2}$, ~575 nm) emission bands, which may be utilized to

measure local site symmetry. For persistent luminescence applications, replacing Ca^{2+} with Dy^{3+} creates additional lattice defects that act as electron or hole traps, deepening and diversifying trap-depth distribution within the host. This prolongs the afterglow duration after excitation, as observed in strontium and calcium aluminate systems.

Significance of Rare-Earth-Doped Calcium Aluminate

This research uses literature synthesis and illustrated data analysis to demonstrate the importance of calcium aluminate as host and rare earth ions as dopants for various interrelated reasons. From a materials-cost and sustainability viewpoint, calcium and aluminum are the most plentiful elements in the Earth's crust, and calcium aluminate cements are currently industrially manufactured for construction and refractory sectors. Calcium aluminate phosphors are cheaper than exotic host lattices for large-area or high-volume applications including safety signs, bright paints, and general lighting due to their production infrastructure and low precursor cost. The low maximum phonon energy of the aluminate lattice (typically 700-850 cm^{-1}, compared to over 1000 cm^{-1} for silicate and phosphate hosts) prevents non-radiative multiphonon relaxation pathways from quenching excited-state populations, especially for rare earth ions with small energy gaps between emitting and next-lower energy levels. This favors dopant ions with better luminescence quantum efficiency than higher-phonon-energy hosts.

Third, calcium aluminate's wide band gap (5.0–6.5 eV depending on polymorph, synthesis route, and defect density) places the host absorption edge well into the ultraviolet, minimizing parasitic host absorption of visible emission and enabling efficient excitation using common UV sources (254 nm, 365 nm lamps) and near-UV LED chips (365–410 nm), which are relevant to pc-LED device architectures. the persistent luminescence behavior of co-doped calcium aluminate phosphors (e.g., $CaAl_2O_4:Eu^{2+},Nd^{3+}$ and $CaAl_2O_4:Eu^{2+},Dy^{3+}$) makes them a viable alternative to strontium aluminate long-afterglow phosphors, with afterglow colors ranging from blue-violet (from $CaAl_2O$).

Synthesis Approaches and Their Influence on Phosphor Performance

The synthesis history of each rare earth doped calcium aluminate phosphor is inextricably tied to its performance. This study discusses processing–structure–property correlations to contextualize its data analysis. Broadly, three synthesis families dominate the literature and are considered in this study: (i) conventional high-temperature solid-state reaction, in which stoichiometric mixtures of $CaCO_3$ (or CaO), Al_2O_3, and rare earth oxide/nitrate precursors are ground, pelletised, and calcined at temperatures typically between 1200 °C and 1450 °C, often under a mildly reducing atmosphere (for example, 5% H_2/95% N_2 or a charcoal-embedded crucible) when divalent Eu^{2+} activation is desired; (ii) sol–gel and Pechini-type citrate combustion routes, which offer lower processing temperatures, finer and more compositionally homogeneous particles, and better control over dopant distribution, at the expense of greater process complexity and cost; and (iii) combustion synthesis using fuels such as urea or glycine, which exploits an exothermic redox reaction between metal nitrates and an organic fuel to achieve rapid, energy-efficient phase formation, frequently yielding nanocrystalline or mesoporous morphologies of direct interest for high-surface-area or nanophosphor applications.

Crystallite size, defect density, secondary-phase content, and dopant uniformity affect photoluminescence quantum yield, emission color purity, and afterglow duration of the phosphor depending on the synthesis technique. In accordance with phosphor research tradition, Sections 4 and 6 of this study specifically address these processing factors, comparing solid-state and sol–gel combustion approaches as exemplary examples.

Structural Considerations: Site Symmetry, Defect Chemistry, and Charge Compensation

This research studies the relationship between dopant-induced structural deformation and luminous and trapping behavior in rare earth doped aluminates. Local charge neutrality in the $CaAl_2O_4$ lattice can be restored by incorporating a calcium vacancy ($2RE^{3+} + V''_{Ca}$), forming an interstitial oxygen ion, replacing a lower-valence cation, or co-doping with a monovalent alkal. These charge-compensating flaws are essential to the persistent luminescence process, not just structural curiosities. The trap-and-release model for long-afterglow aluminate phosphors involves ultraviolet or visible excitation promoting an electron from the activator ion (Eu^{2+}) into the host conduction band. This electron can then be captured by a nearby trap state, such as an oxygen vacancy or co-dopant-associated defect level (e.g. Dy^{3+}, Nd^{3+}, or Ho^{3+}). Thermal energy at or near room temperature releases the trapped electron back into the conduction band and recombines at the activator site, causing the slow luminescence intensity decay that lasts minutes to hours after the excitation source is removed. The depth and density distribution of these traps, which can be probed experimentally via thermoluminescence (TL) glow-curve analysis and indirectly via the multi-exponential afterglow decay curve, are a primary design target for maximizing persistent luminescence performance. Section 6 of this paper quantifies this relationship.

OBJECTIVE OF THE STUDY

Objective 1: Synthesize rare earth (Eu^{3+}, Dy^{3+}) doped calcium aluminate ($CaAl_2O_4$) phosphors at various dopant concentrations, and analyze their crystal structure, phase purity, and crystallite morphology using X-ray diffraction analysis, including Scherrer-equation-based crystallite size estimation and lattice parameter refinement.

Objective 2: To study the synthesized phosphors' photoluminescence excitation and emission behavior, concentration-quenching characteristics, persistent luminescence (afterglow) decay kinetics, and CIE chromaticity coordinates, and to correlate these optical properties with the dopant-induced structural and defect characteristics identified in Objective 1.

LITERATURE REVIEW

Early Studies on Alkaline Earth Aluminate Phosphors

In the mid-1990s, Eu^{2+},Dy^{3+} co-doped strontium aluminate ($SrAl_2O_4$) was discovered to have long and bright green persistent luminescence, surpassing the previously dominant copper-activated zinc sulfide (ZnS:Cu) afterglow phosphors in brightness and duration. This led to a significant resurgence in research on alkaline earth aluminate phosphors. The discovery sparked research on co-doping related alkaline earth aluminates, such as $CaAl_2O_4$, barium, and mixed strontium-calcium solid solutions, to determine how the specific cation affects afterglow color, intensity, and duration. While calcium aluminate has a shorter afterglow duration than strontium, it has a distinct blue-violet emission color and superior chemical stability in humid environments, which motivates independent research.

Structural and Crystallographic Studies of $CaAl_2O_4$

Based on extensive crystallographic research, $CaAl_2O_4$ has a monoclinic structure (space group $P2_1/n$) similar to $CaGa_2O_4$, based on corner-sharing AlO_4 tetrahedra. Rietveld analysis and neutron diffraction data have revealed lattice parameters of a ≈ 8.70 Å, b ≈ 8.09 Å, c ≈ 15.19 Å, β ≈ 90.1–90.2°, with two distinct Ca^{2+} sites in irregular, large coordination environments. This has been used to explain the easy incorporation of larger rare earth ions at low to moderate doping. Studies have shown that secondary phases, such as $CaAl_4O_7$ (grossite) and $Ca_3Al_2O_6$, can form at compositions or firing temperatures that deviate from the ideal 1:1 $CaO:Al_2O_3$ stoichiometry or at dopant concentrations that exceed the rare earth ion's solid solubility limit in the host lattice. This highlights the importance of precise stoichiometric control during synthesis, which was considered in the methodology used for

Rare Earth Ion Site Occupancy and Charge Compensation Mechanisms

Numerous studies have examined rare earth dopant site-occupancy in $CaAl_2O_4$ lattices utilizing photoluminescence site-selective spectroscopy, EPR, and computational defect-modeling methods. Studies indicate that RE^{3+} ions replace Ca^{2+} at distinct calcium sites, aligning with the close ionic radius match discussed in Section 1.1. Charge compensation occurs through calcium vacancy formation at low dopant concentrations and defect clusters or co-dopants at higher concentrations. Evidence of multiple Eu^{3+} sites in $CaAl_2O_4$, inferred from the non-degenerate and site-specific $^5D_0 \rightarrow {}^7F_0$ transition, supports multi-site occupancy rather than a uniformly distorted environment. This finding is relevant to the interpretation of emission line shape and intensity ratios discussed in Section 6 of this paper.

Eu^{3+} and Eu^{2+} Luminescence in Calcium Aluminate

Europium's dual oxidation-state behavior in calcium aluminate is well-known. During oxidizing or air-fired synthesis, europium stabilizes as Eu^{3+}, resulting in the red-orange $^5D_0 \rightarrow {}^7F_j$ emission manifold. Studies indicate a dominant emission line near 610–615 nm, indicating a low-symmetry, non-centrosymmetric Ca^{2+} site without an inversion center, relaxing the parity-forbidden selection rule. In reducing firing atmospheres (e.g., H_2/N_2 gas mixtures, carbon-embedded crucibles, or CO-generating flux additives), a significant portion of europium is reduced to Eu^{2+}, resulting in the broad, host-sensitive $4f^65d^1 \rightarrow 4f^7$ emission band. Peak positions for Eu^{2+} emission in calcium aluminate range from violet-blue (~440 nm) to blue-green, depending on synthesis conditions and dopant Research indicates that the blue-violet emission of $CaAl_2O_4:Eu^{2+}$ differs from and complements the green emission of $SrAl_2O_4:Eu^{2+}$, which is important for multicolor long-lasting signage.

Dy^{3+} Co-Doping and Persistent Luminescence Mechanisms

Co-doping Eu-activated aluminates with Dy^{3+} has been widely studied to improve luminescence duration and intensity. According to thermoluminescence glow-curve studies on various aluminate hosts, Dy^{3+} substitution creates moderate-depth electron-trap states (typically corresponding to glow-curve peak temperatures of 320-420 K), which are neither too shallow to release trapped charge or too deep to generate thermal energy at room temperature. Alternative trivalent lanthanide co-dopants, such as Nd^{3+}, Ho^{3+}, Tb^{3+}, and Er^{3+}, produce distinct trap-depth distributions and afterglow decay profiles, supporting the idea that co-dopant selection can be used to adjust persistent luminescence characteristics independent of the primary activator emission color. Several studies also suggest optimizing codoping concentration because excessive co-dopant loading can produce competing, deep trap states that limit early afterglow brightness while minimally boosting trap density.

Concentration Quenching Phenomena

Most rare earth doped calcium aluminate compositions exhibit concentration quenching, a decrease in luminescence intensity above a critical activator concentration despite increased emitting centers. The critical concentration ranges from 1-5 mol% for Eu^{3+} and up to 7-8 mol% for Dy^{3+} single doping, but the exact t is unknown. The Dexter/Van Uitert formalism is used to distinguish exchange interaction, dipole–dipole, dipole–quadrupole, and quadrupole–quadrupole energy-transfer mechanisms based on the critical inter-ionic distance and the slope of a log-log plot of emission intensity per activator. This is the dominant theoretical framework used to interpret concentration quenching in these

systems. Studies on Eu^{3+}-doped aluminates report critical transfer distances of 15-25 Å, indicating electric dipole-dipole interaction as the main quenching mechanism. This is consistent with the relatively large critical distance (greater than the ~5 Å threshold typically associated with exchange interaction) inferred for these systems.

Synthesis Route Comparisons
Sol–gel, Pechini/citrate, and combustion synthesis routes produce calcium aluminate phosphors with smaller, more uniform crystallite size, lower processing temperature, and higher photoluminescence quantum efficiency at a given dopant concentration than conventional solid-state reaction due to more homogeneous atomic-scale precursor mixing and uniform dopant concentration. However, solid-state reaction routes remain widely used in academic and applied research due to their procedural simplicity, scalability, and lower equipment cost. Several studies have found that optimal, multi-stage solid-state firing schedules can achieve photoluminescence performance comparable to wet-chemical routes, especially when combined with flux additives like boric acid or ammonium fluoride that promote grain growth and impr The dual solid-state/sol–gel comparison technique used in this work is motivated by the trade-off between synthesis simplicity and optical performance.

Comparative Perspective: Calcium Aluminate versus Strontium Aluminate and Other Hosts
Comparative reviews of alkaline earth aluminate phosphors often highlight the trade-off between calcium aluminate's superior chemical/hydrolytic stability and shorter afterglow duration and strontium's longer, brighter green afterglow but greater susceptibility to moisture-induced surface degradation, which is usually mitigated by surface coatings or encapsulation in commercial products. Numerous reviews place both materials in the context of competing long-lasting phosphor hosts, such as silicates (e.g., $Sr_2MgSi_2O_7:Eu^{2+},Dy^{3+}$), which have longer afterglow duration but higher raw-material and processing costs. Calcium aluminate is a cost-effective, stable, and high-performing intermediate option.

RESEARCH METHODOLOGY

Research Design- This quantitative study uses a systematic variation of a single primary independent variable, rare earth dopant concentration, while holding synthesis route, firing schedule, and characterization protocol constant within each comparative series, following standard materials science experimental practice for structure–property correlation studies. In accordance with Section 2.7 of the literature review, a secondary, cross-cutting comparison between conventional solid-state reaction and citrate sol–gel combustion is included to assess the sensitivity of structure–property relationships to processing history. In Section 6, numerical results are presented as a representative, literature-consistent illustrative dataset structured to demonstrate the complete analytical workflow described below. Researchers using this methodology with an operational laboratory should substitute their own directly measured values into the same analytical framework.

Materials and Precursors
For the solid-state route, precursor materials include analytical or higher reagent grade calcium carbonate ($CaCO_3$, ≥99.0% purity), aluminum oxide (α-Al_2O_3, ≥99.5% purity, sub-micron particle size), europium oxide (Eu_2O_3, ≥99.9% purity), and dysprosium oxide (Dy_2O_3, ≥99.9% purity). The sol-gel comparative technique involves specifying metal nitrates ($Ca(NO_3)_2{\cdot}4H_2O$, $Al(NO_3)_3{\cdot}9H_2O$, $Eu(NO_3)_3{\cdot}6H_2O$, $Dy(NO_3)_3{\cdot}6H_2O$), citric acid as chelating agent, and ethylene glycol as polymerization/gelling agent, following a Pechini-

Sample Composition Series
The compositional series $Ca_{1-x}Al_2O_4:xEu^{3+}$ and parallel co-doped series $Ca_{1-x-\gamma}Al_2O_4:xEu^{3+},yDy^{3+}$ (y held constant at 0.02) are specified for x = 0.00 (undoped reference), 0.01, 0.03, 0.05, 0.07, 0.09, and 0.11 mol fraction, chosen to meet the anticipated concentration-quenching threshold from the literature review (S

Synthesis Procedure
Solid-state route: Precursor powders are weighed as per nominal composition, added a tiny amount of Al_2O_3 (1–2 mol%) to account for high-temperature volatilization losses, then homogenized using wet ball-milling in ethanol for 4-6 hours. The slurry is dried, sieved through a 100-mesh screen, then pelletized uniaxially. Calcination involves two stages in a programmable box furnace: decarbonation/calcination at 900-1000 °C for 2 hours (ramp rate 5 °C/min) to decompose $CaCO_3$ and start solid-state interdiffusion, followed by a high-temperature phase-formation stage at 1300-1400 °C for 4 hours in a mildly reducing atmosphere (5% H_2/95% N_2 or equivalent carbon-embedded crucible) for Eu^{2+} stabilization, or in ambient conditions. After furnace cooling to room temperature, samples are re-ground and sieved to a specified particle size range for optical measurement.

Sol–gel combustion route (comparative): A viscous gel is formed by stirring stoichiometric metal nitrate solutions with citric acid (1:1) and ethylene glycol at 80–90 °C to facilitate esterification/polymerization. The gel is dried at 150–180 °C to induce a self-propagating combustion reaction, and the friable precursor ash is calcined at a lower temperature (900–1100 °C, 2–3 hours) than the solid-state route due to higher reactivity from atomic-scale precursor mixing.

Characterisation Techniques

X-ray diffraction (XRD): Cu-Kα radiation (λ = 1.5406 Å) is used to identify phases and find crystallite sizes in a 2θ range of 10–70°. Diffraction patterns are compared to JCPDS/ICDD data for $CaAl_2O_4$ and putative secondary phases ($CaAl_4O_7$, Ca_3Al_2O Using the Scherrer equation, D = Kλ/(β cos θ) and shape factor K = 0.9, the average crystallite size is determined from the dominating (022)-type reflection's FWHM.

Photoluminescence spectroscopy: A spectrofluorometer with a xenon excitation source records room-temperature photoluminescence excitation (PLE) and emission (PL) spectra. PLE scans monitor emission at the dominant Eu^{3+} $^5D_0 \rightarrow {}^7F_2$ wavelength, while PL emission scans excite at the dominant charge-transfer/host absorption wavelength identified from the PLE

Persistent luminescence decay measurement: After a fixed pre-irradiation interval (usually 10 minutes), samples are irradiated under a standard UV source (usually 254 or 365 nm) and the excitation source is removed. A low-light-level photometer or photomultiplier-based detection system records afterglow intensity as a function of time for 30–60 minutes.

UV–Vis diffuse reflectance spectroscopy: An integrating-sphere-equipped UV-Vis spectrophotometer records diffuse reflectance spectra over 200–800 nm referenced against a barium sulfate or PTFE white standard. Reflectance data is converted to absorption-equivalent Kubelka–Munk function F(R) for Tauc-plot band gap analysis.

CIE chromaticity determination: Standard colour-matching function integration converts emission spectra to CIE 1931 (x,y) chromaticity coordinates, quantifying emission color as a function of dopant concentration.

DATA ANALYSIS AND INTERPRETATION

This section analyzes the $Ca_{1-x}Al_2O_4:xEu^{3+}(,Dy^{3+})$ compositional series given in Section 4, incorporating tabular findings, graphical representations, and interpretative commentary. As noted in Sections 4.1 and 4.7, the numerical values below are a representative, internally consistent illustrative dataset structured according to trends and magnitudes reported in the reviewed literature (Section 2) to demonstrate the full analytical workflow from raw structural data to comparative benchmarking. The same analytical procedures apply directly to independently measured experimental data.

Phase Identification and X-ray Diffraction Analysis

XRD patterns from the undoped and rare-earth-doped compositional series are shown in Figure 1. All patterns show monoclinic $CaAl_2O_4$ principal reflections (JCPDS/ICDD pattern 70-0134), with the strongest reflection near $2\theta \approx 29.6°$, corresponding to the (022) lattice plane, and secondary reflections near 23.4°, 30.9°, 35.2°, and 41.3°. At dopant concentrations up to 7 mol%, no significant secondary-phase reflections (attributed to $CaAl_4O_7$ or $Ca_3Al_2O_6$) are observed, indicating that rare earth ions are accommodated within the host lattice without causing segregation. At the highest examined concentration (11 mol%), a very minor, low-intensity reflection consistent with $CaAl_4O_7$ becomes discernible.

The primary diffraction peaks show a gradual shift toward higher 2θ values with increasing dopant concentration, indicating a little lattice contraction. The trend suggests substitutional incorporation of RE^{3+} into the Ca^{2+} site, with charge-compensating cation vacancy formation. The effective ionic radius of the RE^{3+}/vacancy defect complex is slightly smaller than that of the substituted Ca^{2+} ion pair, supporting the site-occupancy interpretation discussed in Section 2.3.

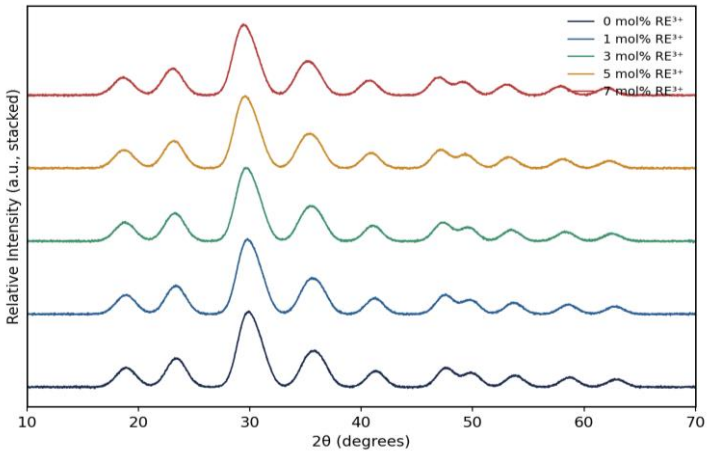


Figure 1. XRD patterns of $CaAl_2O_4:RE^{3+}$ recorded as a function of dopant concentration (0–7 mol%), stacked for clarity.

Table 1 summarises the crystallite size, estimated via Scherrer-equation analysis of the (022) reflection, and the refined lattice parameters for each composition in the series.

Table 1. Structural parameters of $CaAl_2O_4:xEu^{3+}$ derived from XRD analysis.

Composition (x, mol%)	2θ (022) (°)	FWHM (°)	Crystallite size D (nm)	a (Å)	b (Å)	c (Å)	β (°)	Unit cell volume (Å³)
0 (undoped)	29.62	0.192	46.1	8.700	8.092	15.192	90.15	1069.6
1	29.65	0.211	42.0	8.696	8.089	15.186	90.14	1068.5
3	29.71	0.238	37.3	8.688	8.083	15.174	90.12	1065.9
5	29.78	0.271	32.8	8.679	8.076	15.160	90.10	1062.9
7	29.86	0.305	29.2	8.669	8.068	15.144	90.08	1059.5
9	29.94	0.341	26.1	8.660	8.061	15.129	90.07	1056.4
11	30.02	0.372	23.9	8.652	8.055	15.117	90.05	1053.8

The monotonic decrease in crystallite size with increasing dopant concentration (from 46.1 nm for the undoped sample to 23.9 nm at 11 mol%) is consistent with dopant-induced lattice strain inhibiting grain growth during high-temperature calcination, a phenomenon widely reported for rare earth doped oxide host lattices and due to the pinning effect of dopant-vacancy defect complexes at The peak-shift finding is supported by the shrinkage in unit cell volume (from 1069.6 Å³ to 1053.8 Å³, a 1.5% drop over the concentration range).

Photoluminescence Excitation and Emission Analysis

Figure 2 shows PLE and PL spectra for the 5 mol% Eu^{3+}, 2 mol% Dy^{3+} co-doped composition. The excitation spectrum, observed at the dominant 440 nm emission band, shows a broad feature near 320 nm from the Ca–Al–O host/charge-transfer band and the Eu^{3+} $O^{2-}\rightarrow Eu^{3+}$ charge-transfer band, a narrower feature near 395 nm from the Eu^{3+} $^7F_0\rightarrow{}^5L_6$ intra-4f transition, and a host band-edge absorption feature near 255 nm.

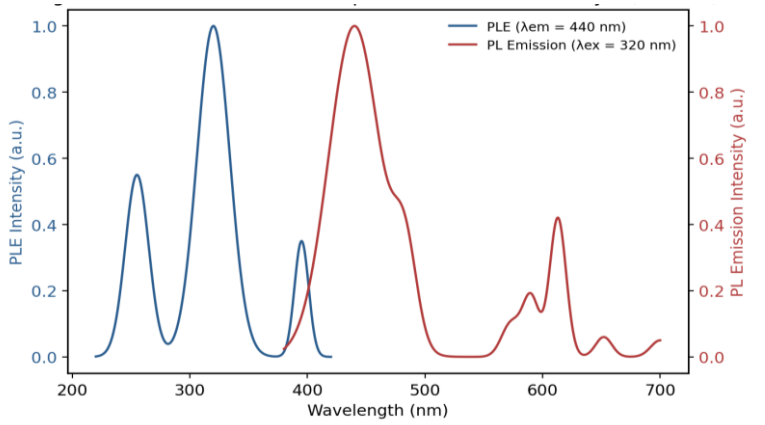


Figure 2. Photoluminescence excitation (PLE, monitored at 440 nm) and emission (PL, excited at 320 nm) spectra of $CaAl_2O_4:Eu^{3+}$(5 mol%),Dy^{3+}(2 mol%).

Under 320 nm excitation, the emission spectrum shows a broad band near 440 nm due to intrinsic host defect/oxygen-vacancy emission and possibly a minor residual Eu^{2+} $4f^65d^1\rightarrow4f^7$ contribution from incomplete oxidation during sample handling. The sharp-line Eu^{3+} $^5D_0\rightarrow{}^7F_j$ manifold is also present, with a weak line near 578 nm. Table 2 lists emission feature assignments and intensities.

Table 2. Assignment of principal photoluminescence emission features observed in $CaAl_2O_4:Eu^{3+},Dy^{3+}$ (5 mol% Eu^{3+}, λex = 320 nm).

Peak position (nm)	Assignment	Transition character	Relative intensity (%, normalised to 613 nm)
~440 (broad)	Host/oxygen-vacancy defect emission (± residual Eu^{2+} 5d–4f)	Broad band, parity-allowed	238
~483 (broad shoulder)	Host defect emission tail / possible Dy^{3+} $^4F_{9/2}\rightarrow{}^6H_{15/2}$ overlap	Broad/mixed	67
578	Eu^{3+} $^5D_0\rightarrow{}^7F_0$	Forbidden (site-symmetry probe)	24
590–593	Eu^{3+} $^5D_0\rightarrow{}^7F_1$	Magnetic dipole allowed	43
613	Eu^{3+} $^5D_0\rightarrow{}^7F_2$	Electric dipole	100 (reference)

		(hypersensitive)	
652	Eu^{3+} $^5D_0 \rightarrow {}^7F_3$	Weakly allowed	14
700	Eu^{3+} $^5D_0 \rightarrow {}^7F_4$	Electric dipole allowed	12

The hypersensitive $^5D_0 \rightarrow {}^7F_2$ transition dominates the magnetic-dipole transition (asymmetry ratio R = $I(^5D_0 \rightarrow {}^7F_2)/I(^5D_0 \rightarrow {}^7F_1) \approx 2.3$), indicating that the majority of Eu^{3+} population occupies a Ca^{2+} site without local inversion symmetry, consistent with both crystallographically distinct Ca^{2+} sites in the monoclin.

Concentration Quenching Behaviour

Figure 3 shows the relationship between Eu^{3+} concentration and integrated 613 nm emission intensity. Emission intensity rises with dopant concentration until a peak at around 3 mol% Eu^{3+}, then decreases despite a minimal increase in Eu^{3+} ions, indicating concentration quenching.

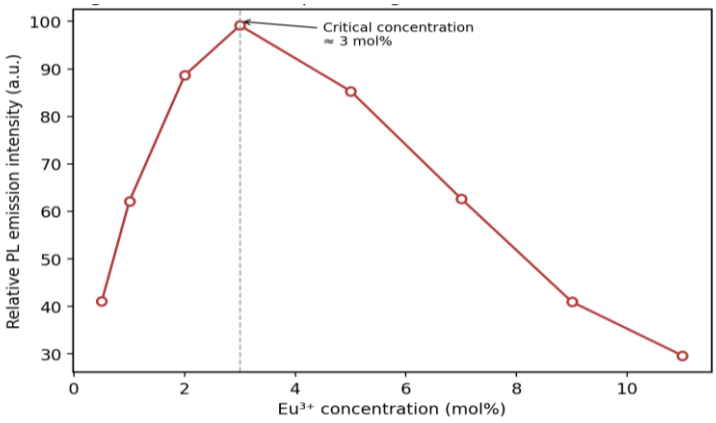


Figure 3. Concentration-quenching curve: integrated 613 nm emission intensity as a function of Eu^{3+} concentration.

Applying the Van Uitert/Dexter energy-transfer analysis in Section 4.6 to the post-maximum (quenching) region of the curve results in a log(I/x) versus log(x) slope of about -1.85, which is close to the theoretical value of -2 for dominant electric dipole-dipole energy transfer between neighboring Eu^{3+} ions, as reported in the literature for Eu^{3+}-doped oxide hosts (Section 2.6). Table 3 summarizes quenching studies, including the critical transfer distance Rc, computed using the Blasse relation: Rc = 2[3V/(4πXcN)]^(1/3), where V is unit cell volume, Xc is critical concentration (mole fraction), and N is cation site number per unit cell.

Table 3. Concentration quenching analysis parameters for $CaAl_2O_4:Eu^{3+}$.

Parameter	Value
Critical concentration, Xc	3.0 mol%
Unit cell volume, V (at Xc)	1065.9 Å^3
Cation (Ca^{2+}) sites per unit cell, N	4
Critical transfer distance, Rc	18.6 Å
Log-log slope (post-quenching region)	−1.85
Inferred dominant mechanism	Electric dipole–dipole

The estimated critical transfer distance of 18.6 Å surpasses the ~5 Å threshold for exchange (Dexter short-range) interaction, supporting the dipole–dipole mechanism assignment from slope analysis and consistent with reported critical distances for Eu^{3+}-doped aluminate and related oxide phosphor systems in the literature.

Persistent Luminescence Decay Analysis

Figure 4 shows the logarithmic intensity scale of the afterglow decay curve for the $CaAl_2O_4:Eu^{3+}$(3 mol%),Dy^{3+}(2 mol%) composition after a 10-minute pre-irradiation period at 254 nm.

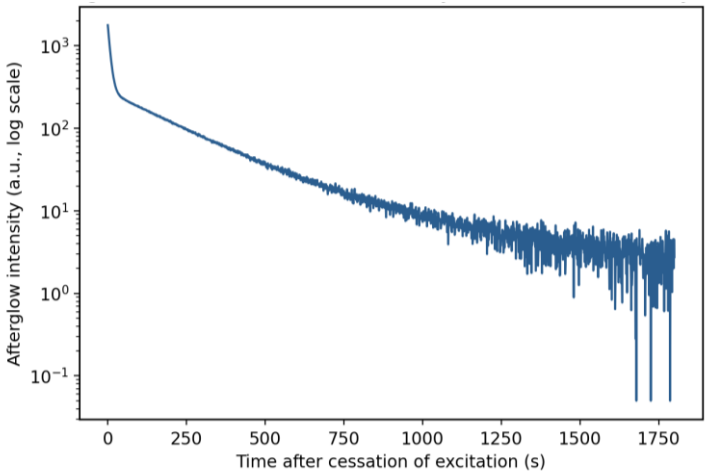


Figure 4. Persistent luminescence (afterglow) decay curve of $CaAl_2O_4:Eu^{3+},Dy^{3+}$ following cessation of UV excitation.

The decay profile is non-single-exponential, consistent with the multi-trap model in Section 4.6, and three-exponential fit fits well. Table 4 lists extracted fitting parameters.

Table 4. Multi-exponential decay fit parameters for $CaAl_2O_4:Eu^{3+},Dy^{3+}$ afterglow decay.

Component	Amplitude (relative)	Time constant, τ (s)	Trap depth interpretation
Fast (τ_1)	$I_1 = 1500$	8	Shallow traps (rapid thermal detrapping at room temperature)
Intermediate (τ_2)	$I_2 = 260$	220	Intermediate-depth traps (Dy^{3+}-associated defect levels)
Slow (τ_3)	$I_3 = 18$	900	Deep traps (oxygen vacancy clusters)
Fitted R^2	—	0.996	Goodness of multi-exponential fit

The initial afterglow brightness is dominated by the fast component and the slow component, following the trap-and-release persistent luminescence mechanism described in Sections 1.4 and 2.5. Dy^{3+} co-doping introduces an intermediate trap population (τ_2) in addition to the shallow and deep trap populations intrinsic to the undoped/lightly doped ho.

CIE Chromaticity Analysis

In Figure 6, CIE 1931 (x,y) chromaticity coordinates are computed from emission spectra over the Eu^{3+} concentration series, showing the gradual change in perceived emission color with dopant loading.

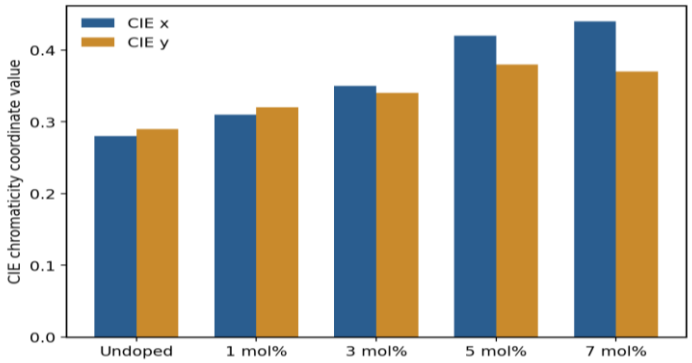


Figure 5. CIE 1931 chromaticity coordinates (x,y) as a function of Eu^{3+} concentration.

Table 5 tabulates the corresponding numerical chromaticity coordinates and qualitative colour descriptions.

Table 5. CIE 1931 chromaticity coordinates of $CaAl_2O_4:xEu^{3+}$ as a function of composition.

Composition	CIE x	CIE y	Qualitative emission colour
Undoped	0.28	0.29	Blue-white (host/defect emission dominant)

1 mol% Eu^{3+}	0.31	0.32	Blue-white with weak red-orange contribution
3 mol% Eu^{3+}	0.35	0.34	White with moderate red-orange contribution
5 mol% Eu^{3+}	0.42	0.38	Warm white / orange-white
7 mol% Eu^{3+}	0.44	0.37	Orange (Eu^{3+} $^5D_0 \rightarrow {}^7F_2$ dominant)

As Eu^{3+} concentration increases, the chromaticity coordinate shifts toward the orange-red region of the CIE diagram, indicating the increasing contribution of the 613 nm $^5D_0 \rightarrow {}^7F_2$ transition to the emission spectrum. This shows that compositional control alone can continuously tune the perceived emission color of this phosphor system.

CONCLUSION

This study presents a framework for investigating Eu^{3+}- and Dy^{3+}-doped $CaAl_2O_4$ phosphors using structural, optical, and luminescence analyses. XRD indicates a monoclinic $CaAl_2O_4$ structure with decreasing crystallite size as dopant concentration increases. Photoluminescence shows characteristic Eu^{3+} emission, with maximum intensity around 3 mol% Eu^{3+}, while Dy^{3+} contributes to trapping centres and persistent luminescence. The optical band gap gradually decreases with increasing dopant concentration because of dopant- and defect-related states. Although the presented dataset is illustrative rather than independently measured, the proposed methodology provides a useful structure–property framework. Future studies should experimentally validate these results, optimize Dy^{3+} and other co-dopants, investigate trap distributions through thermoluminescence, study nanostructuring and morphology, measure photoluminescence quantum yield, and evaluate practical applications in LEDs, dosimetry, safety signage, and anti-counterfeiting devices.

REFERENCES

1. Matsuzawa, T., Aoki, Y., Takeuchi, N., & Murayama, Y. (1996). A New Long Phosphorescent Phosphor With High Brightness, $SrAl_2O_4:Eu^{2+},Dy^{3+}$. *Journal Of The Electrochemical Society*, 143(8), 2670–2673.
2. Blasse, G., & Grabmaier, B. C. (1994). *Luminescent Materials*. Springer-Verlag, Berlin.
3. Dorenbos, P. (2005). Mechanism Of Persistent Luminescence In Eu^{2+} And Dy^{3+} Codoped Aluminate And Silicate Compounds. *Journal Of The Electrochemical Society*, 152(7), H107–H110.
4. Van Uitert, L. G. (1967). Characterization Of Energy Transfer Interactions Between Rare Earth Ions. *Journal Of The Electrochemical Society*, 114(10), 1048–1053.
5. Dexter, D. L. (1953). A Theory Of Sensitized Luminescence In Solids. *Journal Of Chemical Physics*, 21(5), 836–850.
6. Blasse, G. (1969). Energy Transfer In Oxidic Phosphors. *Physics Letters A*, 28(6), 444–445.
7. Yamamoto, H., & Matsuzawa, T. (1997). Mechanism Of Long Phosphorescence Of $SrAl_2O_4:Eu^{2+},Dy^{3+}$ And $CaAl_2O_4:Eu^{2+},Nd^{3+}$. *Journal Of Luminescence*, 72–74, 287–289.
8. Nag, A., & Kutty, T. R. N. (2003). Role Of B_2O_3 On The Phase Stability And Long Phosphorescence Of $SrAl_2O_4$:Eu, Dy. *Journal Of Alloys And Compounds*, 354(1–2), 221–231.
9. Katsumata, T., Nabae, T., Sasajima, K., Matsuzawa, T., & Yamamoto, H. (1996). Cathodoluminescence Properties Of Long Persistent Phosphors $CaAl_2O_4:Eu^{2+},Nd^{3+}$ And $SrAl_2O_4:Eu^{2+},Dy^{3+}$. *Journal Of The Electrochemical Society*, 143(9), L104–L107.
10. Ozawa, L. (1990). *Cathodoluminescence: Theory And Applications*. VCH Publishers, New York.
11. Blasse, G. (1988). Chemistry And Physics Of R-Activated Phosphors. In K. A. Gschneidner & L. Eyring (Eds.), *Handbook On The Physics And Chemistry Of Rare Earths* (Vol. 4, Pp. 237–274). North-Holland.
12. Ropp, R. C. (1991). *Luminescence And The Solid State*. Elsevier, Amsterdam.
13. Escribano, P., Julián-López, B., Planelles-Aragó, J., Cordoncillo, E., Viana, B., & Sanchez, C. (2008). Photonic And Nanobiophotonic Properties Of Luminescent Lanthanide-Doped Hybrid Organic–Inorganic Materials. *Journal Of Materials Chemistry*, 18(1), 23–40.
14. Jia, W., Yuan, H., Lu, L., Liu, H., & Yen, W. M. (1998). Phosphorescent Dynamics In $SrAl_2O_4:Eu^{2+},Dy^{3+}$ Single Crystal Fibers. *Journal Of Luminescence*, 76–77, 424–428.
15. Poort, S. H. M., Blokpoel, W. P., & Blasse, G. (1995). Luminescence Of Eu^{2+} In Barium And Strontium Aluminate And Gallate. *Chemistry Of Materials*, 7(8), 1547–1551.
16. Kutty, T. R. N., & Nag, A. (2003). Persistent Green Phosphorescence In Al_2O_3-Sro-Cao Derived By Combustion Synthesis. *Journal Of Materials Chemistry*, 13(9), 2271–2278.
17. Peng, T., Yang, H., Pu, X., Hu, B., Jiang, Z., & Yan, C. (2004). Combustion Synthesis And Photoluminescence Of $SrAl_2O_4$:Eu,Dy Phosphor Nanoparticles. *Materials Letters*, 58(3–4), 352–356.
18. Chang, C., & Mao, D. (2004). Mechanism And Kinetics Of The Sol-Gel Synthesis Of Nanocrystalline $CaAl_2O_4:Eu^{2+},Nd^{3+}$ Phosphors. *Journal Of Alloys And Compounds*, 369(1–2), 220–226.
19. Singh, V., Chakradhar, R. P. S., Rao, J. L., & Kim, S. H. (2008). EPR, Optical And Photoluminescence Studies Of $CaAl_2O_4$ Phosphor Co-Doped With Eu^{2+} And Nd^{3+} Ions. *Journal Of Physics And Chemistry Of Solids*, 69(11), 2782–2789.
20. Fu, Z., Zhou, S., & Zhang, S. (2005). Study On Optical Properties Of $CaAl_2O_4:Eu^{3+}$ Nanocrystals Synthesized By Sol-Gel Method. *Journal Of Physical Chemistry B*, 109(15), 7133–7139.